Supporting Information

for

Understanding the interlayer rearrangement toward enhanced lithium storage for LiBC anode

Qianwen Yang[#,a], Langlang Chen[#,a], Zhiyu Liu[a], Yaqing Wei[*,a], De Li[*,a] and Yong Chen[*,b]

a. Q. Yang, L. Chen, Z. Liu, Prof. Y. Wei, Prof. D. Li
State Key Laboratory on Marine Resource Utilization in South China Sea
Hainan Provincial Key Laboratory of Research on Utilization of Si-Zr-Ti Resources
School of Materials Science and Engineering
Hainan University
Haikou 570228, China.
E-mail: yqwei@hainanu.edu.cn; lidenju@sina.com

b. Prof. Y. Chen
Guangdong Key Laboratory for Hydrogen Energy Technologies; School of Materials Science and Hydrogen Energy
Foshan University
Foshan, 528000, China
E-mail: ychen2002@163.com

# Q. Yang and L. Chen contributed equally to this work

Experimental Procedures

Material synthesis

Two LiBC samples were synthesized by a typical solid state reaction. The raw materials for synthesizing LiBC are LiH (≥97.0%, Shanghai Macklin Biochemical Co., Ltd.), amorphous B (≥95.0%, Sigma-Aldrich Co. LLC), graphite (750-850 mesh, 99.99%, Shanghai Aladdin Biochemical Technology Co., Ltd.), and Li foil (≥99.99%， Tianjin Zhongneng Lithium Industry Co., Ltd.). We prepared two LiBC samples as o-LiBC and m-LiBC with raw materials as LiH/B/graphite/Li (1:1:1:5 in mole, wrapped in Li foil) and LiH/B/graphite (1:1:1 in mole), respectively. Actually, the o-LiBC can also be synthesized without Li metal but with superfluous LiH starting material. In an Ar atmosphere, the raw materials of LiH/B/graphite were thoroughly grounded in an agate mortar, pressed into a pellet (wrapped in Li foil for o-LiBC only), sandwiched by two Ta discs, and loaded within a stainless steel vessel, as shown in **Figure 1**. The vessel was sintered at 800 °C for 10h in an electrical tube furnace filled with Ar gas to obtain the LiBC samples. In a glove box with an Ar atmosphere (H_2O, O_2 < 1 ppm), the LiBC samples were taken out from the vessel and stored inside the glove box.

Material characterization

The LiBC samples were characterized by scanning electron microscopy (SEM, Phenom ProX, 10 kV), X-ray photoelectron spectroscopy (XPS, Axis Supra), X-ray powder diffractometer (XRD, Bruker D2 PHASER) with Cu Kα radiation, and Raman imaging microscopy (Thermo fisher Scientific DXRxi) with a laser wavelength of 532 nm. The crystal structures were refined by Rietveld method using the GSAS software package. The High Angle Annular Dark Field Scanning Transmission Electron Microscopy (HAADF-STEM), TEM and Selected Area Electron Diffraction (SAED) were performed on FEI Talos microscope fitted with Super-X EDX system, operated at 200kV. The solid-state $^{7}Li/^{11}B/^{13}C$ magic angle spinning nuclear magnetic resonance (MAS NMR) experiments were performed on a Bruker Advance Ⅲ 600 MHz spectrometer operating at a frequency of 156.4 MHz. The rotating frequency was 14 kHz with a zirconia rotor, and a standard 4 mm HX double-resonance MAS probe was employed. The spectra were recorded with a single pulse excitation using a 90° pulse of 0.5 μs and a recycle delay of 1 s. $^{7}Li/^{11}B/^{13}C$ chemical shifts were referenced by using LiCl, H_3BO_3 and tetramethylsilane (TMS), respectively.

Electrochemical measurements

The electrochemical measurements were conducted for the LiBC samples within a coin-type cell CR2025 that was assembled in a glove box filled with Ar gas (H_2O, O_2 < 1 ppm). The working electrode consisted of 90 wt.% active material LiBC and 10 wt.% adhesive agent polytetrafluoroethylene (Teflons PTFE 610A 470 mm). Such above mixtures were thoroughly ground and firmly pressed in an agate mortar to form a flat paste film, which was punched into small pieces with a diameter of 4 mm. As we described in our previous work, the working electrode was pressed onto a stainless-steel mesh (SUS304) by a pressure of 10 T with a mass loading of ca. 5 mg cm^{-2}. The counter electrode was a Li foil, and a Celgard 2400 separator between two electrodes was immersed in an electrolyte of 1M $LiClO_4$ or 1M $LiPF_6$ dissolved in ethylene carbonate/diethyl carbonate (EC/DEC 1: 1 in volume). At the room temperature of 25 °C, the galvanostatic and electrochemical impedance spectroscopy (EIS) measurements were conducted on a battery charge/discharge system from Hokuto Denko Corp. and an electrochemical workstation (BioLogic VSP-300), respectively.

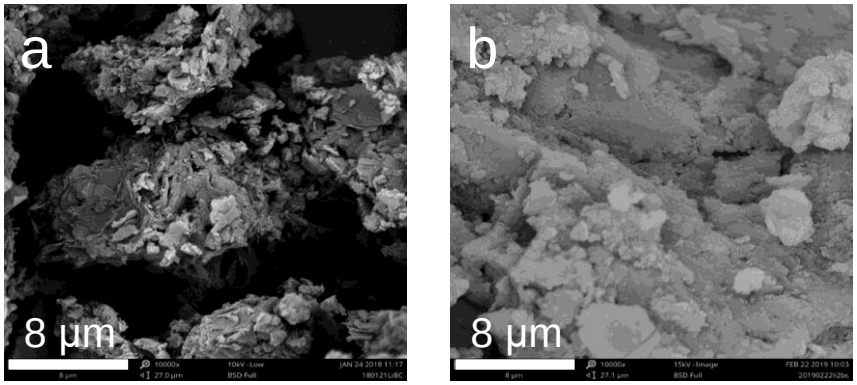

Figure S1. The SEM images of synthesized m-LiBC (a) and o-LiBC (b).

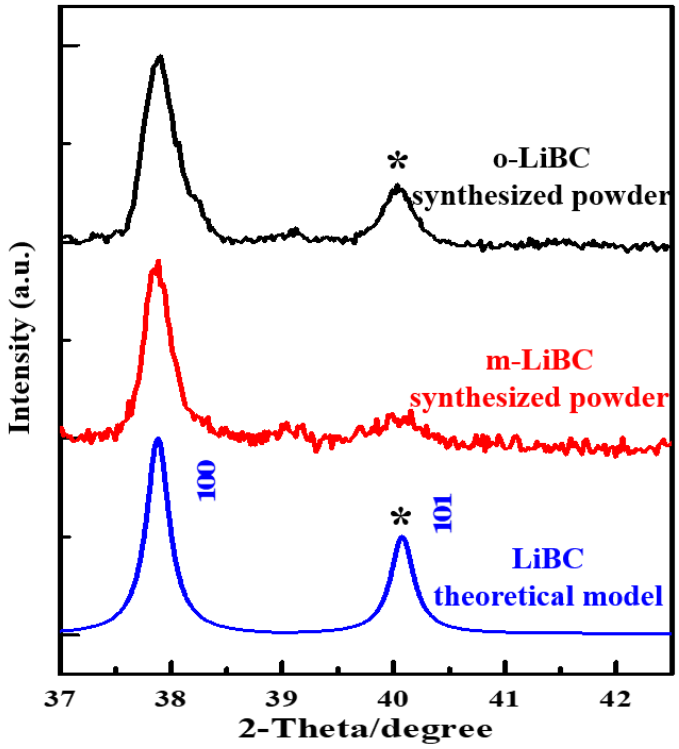

Figure S2. Comparison of the simulated and practical XRD patterns for o-LiBC and m-LiBC.

There is an obvious diffraction peak (101) at ~40.1° for the theoretical LiBC model, in consistent with the synthesized o-LiBC powder. However, this characteristic peak became weaken even disappeared for the m-LiBC. This is because the interlayer defect (e.g. double AA layer) into periodical structure $(AB)_n$ affects the arrangement of (101) plane and thereby, resulting its weaken diffraction signal. Actually, the LiBC structure can be decomposed as two alternative curved layers of only B atoms and only C atoms in the (101) plane and thereby, the (101) peak is influenced by the difference between B and C atoms arrangement in such two curved layers. When the B and C atoms are exchanged after inducing the defective AA layer, the phase of scattered X-Ray will be reversed to counteract with that scattered from the other side. The defective AA layers may divide the LiBC particle into crystalline domains, so the X-Ray scattering by the (101) plane will be counteracted among different domains, resulting in a much weaken (101) peak. Thereby, the m-LiBC model with defective AA layers has been experimentally proved by the fine XRD patterns.

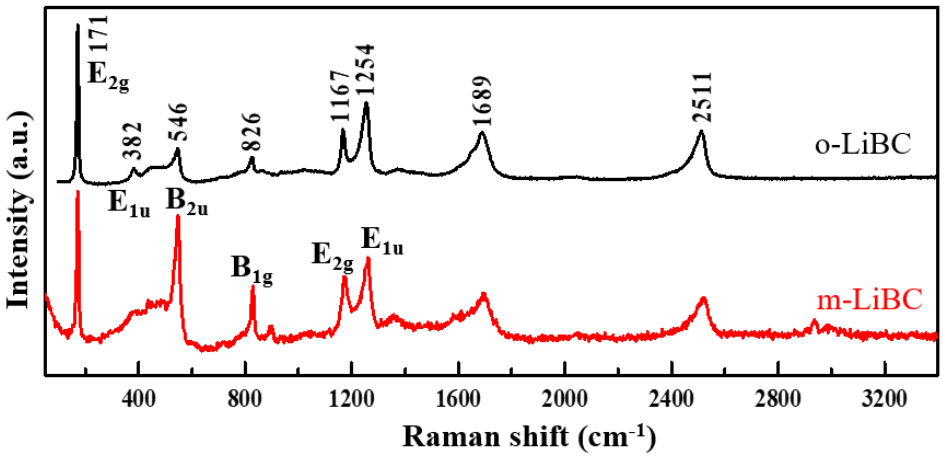

Figure S3. The Raman spectra for o-LiBC and m-LiBC.

There are six bands at 171, 382, 546, 826, 1167 and 1254 cm^{-1} for two LiBC samples, corresponding to E_{2g} (BC planes slide against each other, Li at rest), E_{1u} (Li layers slide against BC layers), B_{2u} (Li layers vibrate against each other along c), B_{1g} (symmetric vibration of BC layers along c, Li at rest), E_{2g} (B-C bond stretching mode, and displacement of BC layers), and E_{1u} (B-C bond stretching mode, odd displacement of BC layers), respectively. The strong asymmetric bands at 1689 cm^{-1} and 2511 cm^{-1} might be attributed to the doubled frequency of the B-C puckering mode and the B-C bond stretching mode, respectively.

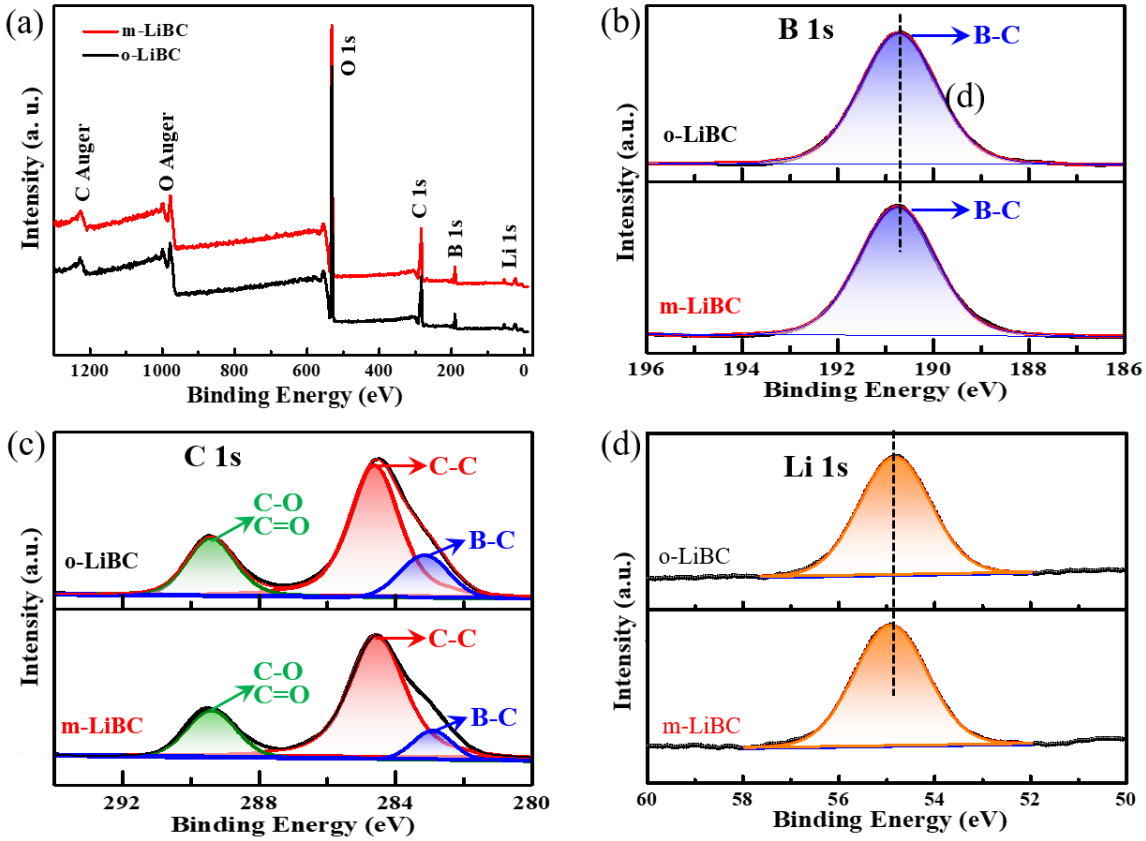

Figure S4 The XPS spectra of the synthesized o-LiBC and m-LiBC samples: (a) survey, (b) B^{1s} (c) C^{1s} and (d) Li^{1s} .

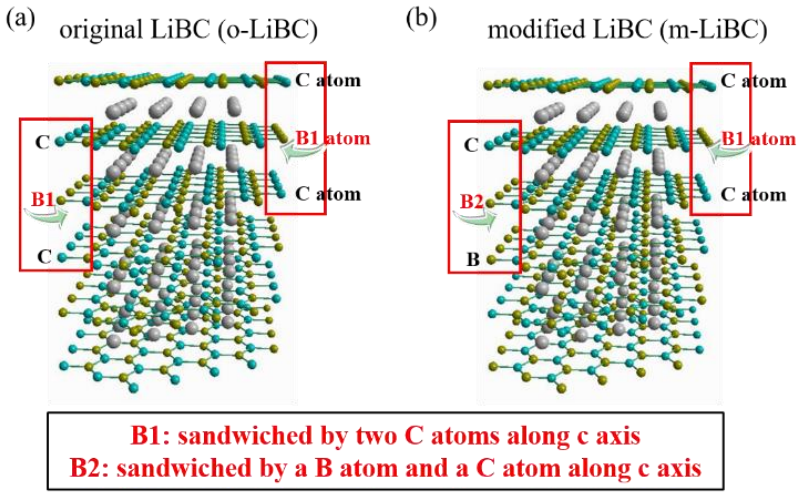

Figure S5 The chemical environments of B atom for o-LiBC (a) and m-LiBC (b).

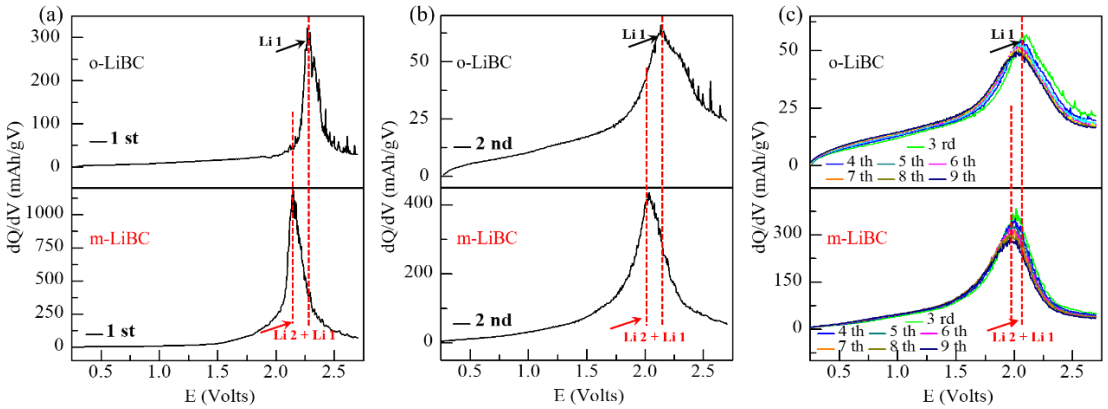

Figure S6. Comparison of the dQ/dV oxidation peaks between o-LiBC and m-LiBC electrodes for the 1st cycle (a), 2nd cycle (b) and following 3rd to 9th cycles (c).

The oxidation dQ/dV peaks of o-LiBC and m-LiBC electrodes are shown in Figure S6a-c. It can be seen that all of the dQ/dV peaks of m-LiBC are shifted to lower potential compared to o-LiBC. Such above phenomenon may be attributed to the existence of Li2 sites in m-LiBC structure. There are two different Li environment (e.g. Li1 and Li2 sites) in m-LiBC, however, their activation/extraction energy and diffusion energy of above Li1 and Li2 sites are too close to distinguish. Therefore, it is hard to separate the Li2 peak from the charging process and thereby, just one oxidation can be observed with obvious potential shifting for the m-LiBC electrode. Considering the potential shifting toward lower values, the activation energy of Li2 site may be slightly lower than that of Li1 site. Nevertheless, the following discharging process further clarified the above two different Li environment since two reduction dQ/dV peaks can be clearly detected.

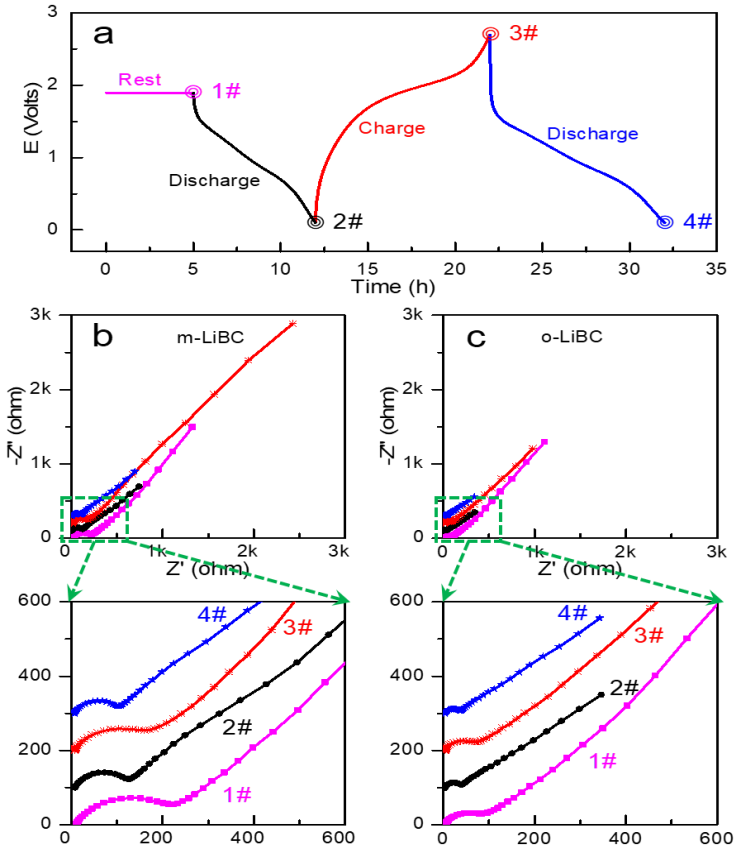

Figure S7 (a) The discharge/charge profiles and electrochemical treatment as rest for 5h (1#), discharge to 0.1 V (2#), charge to 2.7 V (3#) and discharge to 0.1 V (4#). EIS measurements from 2×10^{5} Hz to 10^{-2} Hz and enlarged views at the electrochemical states 1# (magenta), 2# (black), 3# (red) and 4# (blue) for (b) m-LiBC and (c) o-LiBC, where the EIS spectra were collected at the open circuit potential after a rest of 10 minutes.

In the EIS spectra, the semicircle in high frequency could be assigned to the resistance of solid electrolyte interface (SEI) layer, and the tilted line in low frequency is described as the Warburg impedance resulting from the Li-ion migration. For both samples, the semicircle was larger and the tilted line was longer at the charged state (3#) than that at the discharge state (2# and 4#). And the semicircle of o-LiBC was evidently smaller than that of m-LiBC, that is, the resistance of the SEI layer is smaller for o-LiBC, so the low capacity of o-LiBC should not be attributed to the electrical conductivity.

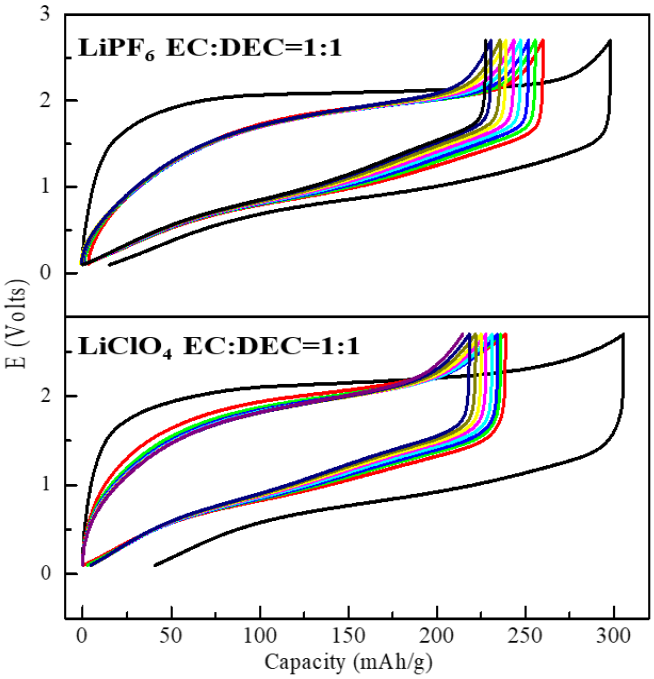

Figure S8. Comparison of the discharge/charge profiles of m-LiBC electrode using $LiClO_4$ and $LiPF_6$ as electrolytes, respectively.

As shown in Figure S8, when using the $LiPF_6$ as electrolyte, the m-LiBC electrode also delivers a large capacity of 235 mAh/g, which is comparable to that of $LiClO_4$ (220 mAh/g). Besides, the m-LiBC electrode using $LiPF_6$ as electrolyte also exhibits superior cycle stability, suggesting the similar electrochemical performances between the $LiClO_4$ and $LiPF_6$. Therefore, the $LiPF_6$ electrolyte also provides the same results and there is no influence on the selection of electrolytes.

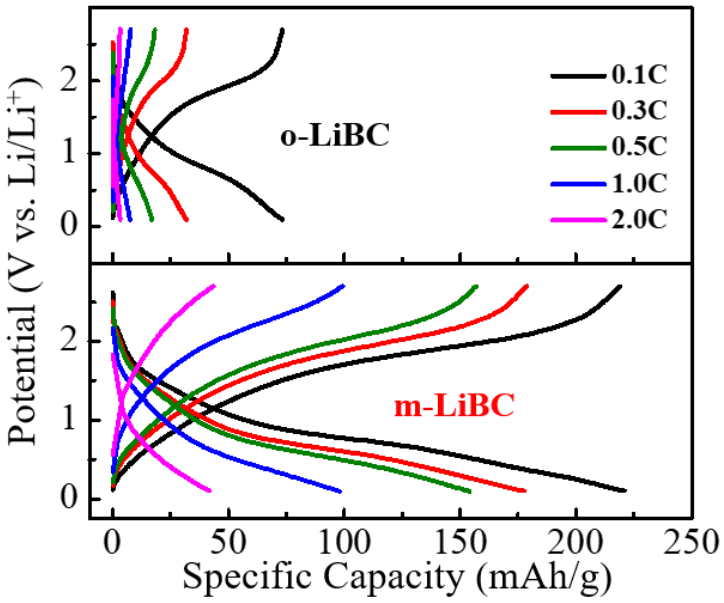

Figure S9. Comparison of the discharge/charge profiles at different current density between the o-LiBC and m-LiBC electrodes.